Understanding Microscopic Operating Mechanisms of a van der Waals Planar Ferroelectric Memristor

Matthew Gabel and Yi Gu*

Ferroelectric memristors represent a promising new generation of devices that have a wide range of applications in memory, digital information processing, and neuromorphic computing. Recently, van der Waals ferroelectric In_2Se_3 with unique interlinked out-of-plane and in-plane polarizations has enabled multidirectional resistance switching, providing unprecedented flexibility in planar and vertical device integrations. However, the operating mechanisms of these devices have remained unclear. Here, through the demonstration of van der Waals In_2Se_3-based planar ferroelectric memristors with the device resistance continuously tunable over three orders of magnitude, and by correlating device resistance states, ferroelectric domain configurations, and surface electric potential, the studies reveal that the resistive switching is controlled by the multidomain formations and the associated energy barriers between domains, as opposed to the commonly assumed Schottky barrier modulations at the metal-ferroelectric interface. The findings reveal new device physics through elucidating the microscopic operating mechanisms of this new generation of devices, and provide a critical guide for future device development and integration efforts.

1. Introduction

Ferroelectric materials, particularly oxides characterized by spontaneous electric polarizations that can be tuned by an external electric field, have found a wide range of applications in random-access memories,[1,2] tunneling junctions,[3] and field-effect transistors.[4] Recent advances include the development of ferroelectric memristors,[5] where the device resistance can be continuously controlled by external signals. Such devices are envisioned to enable solid-state synapses that can be used to mimic brain functions and to implement neuromorphic computing.[6] In all these applications, device miniaturization is a critical element. As the device dimensions continue to shrink, however, the depolarization field, which arises from the surface bound charges, becomes stronger. As a result, the ferroelectricity disappears below a critical thickness; for example, the polarization in $BaTiO_3$ films thinner than ≈2.4 nm is suppressed.[7] In addition, the Curie temperature

becomes lower in general in thinner oxide films,[8,9] presenting a roadblock for device miniaturizations.

Recently, van der Waals ferroelectrics have emerged as potential materials of choice for further advancing ferroelectric device technologies. Robust ferroelectricity in the few- and mono-layer limit has been demonstrated in these materials, including the group-IV monochalcogenides,[10–12] $CuInP_2S_6$, WTe_2, and $MoSe_2$,[13–16] which is desirable for realizing ultrathin devices.[17–20] Furthermore, the van der Waals bonding allows for straightforward integration of ferroelectrics and other materials, for example ferromagnets, providing opportunities to explore novel device concepts such as multiferroics.[21–24] Among newly discovered van der Waals ferroelectrics, α-phase semiconducting In_2Se_3 (α-In_2Se_3) has unique interlinked out-of-plane (OOP) and in-plane (IP) polarizations that are sustained by covalent bonding,[25–31] suggesting that the OOP polarization can be switched via both external OOP and IP electric fields. Based on this unique concept, multidirectional devices such as gate-controlled switchable rectifiers[32] and planar/vertically integrated devices with memristive behaviors[33] have been demonstrated. In these studies, the mechanism underlying the resistive switching was assumed, based on current–voltage relations, to be the modulation of the metal-ferroelectric Schottky barrier controlled by the electric polarization reversal. However, previous studies[34] of ferroelectric capacitors have shown that the resistive switching in these types of devices can be due to non-ferroelectric processes (e.g., defect-related processes), and that current-voltage relations alone are not sufficient to identify ferroelectric processes as the switching mechanism. Furthermore, the novel van der Waals device designs (e.g., planar memristors) might spawn new device physics that is distinct from that in conventional structures.

In this work, we have fabricated planar ferroelectric memristors based on van der Waals α-In_2Se_3; the device resistance can be tuned continuously over three orders of magnitude, demonstrating memristive behaviors. Through a direct correlation among ferroelectric domain configurations, electric potentials, and device resistance states, our studies reveal that the multidomain formation and the in-plane energy barriers between domains, rather than the modulation of the metal-ferroelectric Schottky barriers, are responsible for the resistive switching. These findings uncover new device physics that controls the

M. Gabel, Prof. Y. Gu
Department of Physics and Astronomy
Washington State University
Pullman, WA 99164, USA
E-mail: yigu@wsu.edu

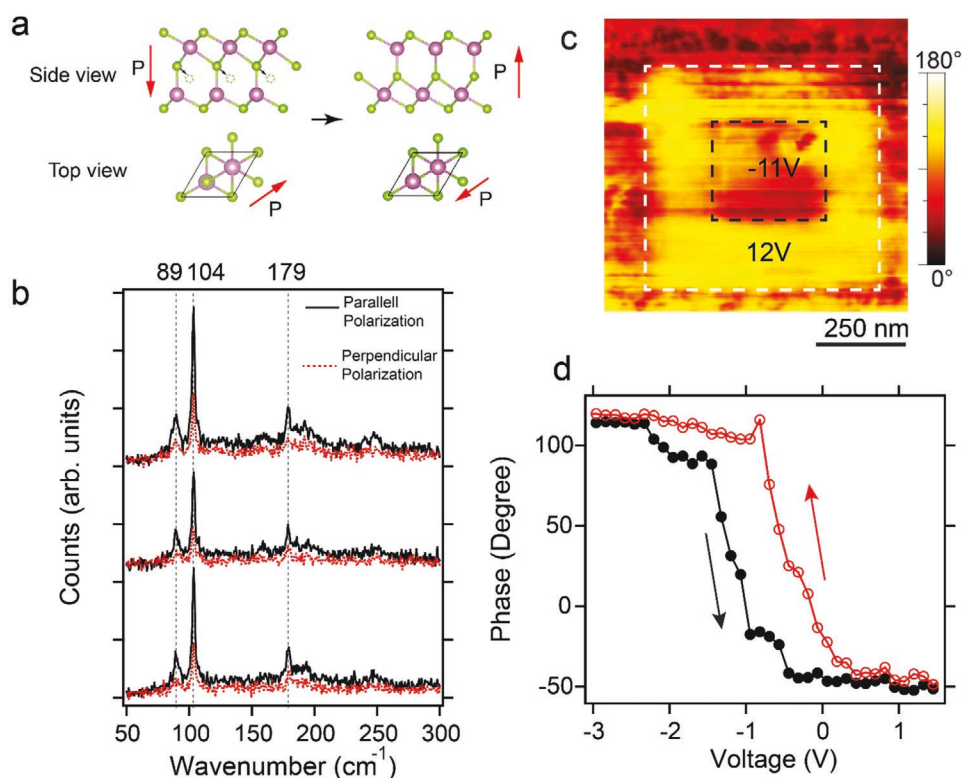The ORCID identification number(s) for the author(s) of this article can be found under https://doi.org/10.1002/adfm.202009999.

**ADVANCED
SCIENCE NEWS**
www.advancedsciencenews.com

**ADVANCED
FUNCTIONAL
MATERIALS**
www.afm-journal.de

Figure 1. Structural and ferroelectric properties. a) Schematic crystal structure of α-In$_2$Se$_3$ with OOP and IP polarizations indicated. b) Polarized Raman spectra (vertically shifted for clarity) taken from three different locations on a single α-In$_2$Se$_3$ layer. c) OOP PFM phase image of an α-In$_2$Se$_3$ layer (thickness ≈45 nm) exfoliated on Au with the outer (inner) box patterned with the 12 V (−11 V) biased AFM tip. d) OOP hysteresis phase loop measured from an α-In$_2$Se$_3$ layer (thickness ≈65 nm) exfoliated on Au.

switching process in the next-generation ferroelectric memristors, and provide an important guide for future device development and integration efforts.

2. Results and Discussion

A monolayer α-In$_2$Se$_3$ consists of five covalent-bonded atomic layers (Se-In-Se-In-Se), as shown in **Figure 1**a. The OOP polarization originates from the uneven spacings between the central Se layer and the neighboring two In layers, which break the centrosymmetry. The shift of the central Se layer into an equivalent position (indicated by dashed circles) reverses the OOP polarization. Accompanying this OOP polarization, there is also a breaking of the in-plane centrosymmetry, resulting in an IP polarization.[29] The unique OOP-IP interlink allows for using an IP electric field to switch the OOP polarization (see also below). Polarized Raman spectroscopy was used to verify the α-phase lattice of exfoliated In$_2$Se$_3$ layers. Particularly, parallel- and perpendicular-polarized Raman spectra, where the polarization condition refers to the orientations between excitation and detection, were obtained from multiple locations from a single layer. As shown in Figure 1b, main Raman peaks corresponding to α-In$_2$Se$_3$ phonon modes can be observed; in particular, the peaks at ≈89, 104, and 179 cm^{-1} can be attributed to an A_1 mode, a combination mode (sum of two E modes), and an A_1 mode, respectively.[35] The intensity of these peaks decreases under

the perpendicular-polarization condition. As such changes are determined by the crystal symmetry, the similar difference between the parallel- and perpendicular-polarization spectra observed at multiple locations indicates the single crystallinity of exfoliated layers.

To probe the ferroelectricity of α-In$_2$Se$_3$ layers, piezoresponse force microscopy (PFM) with local poling was conducted. A box-in-box OOP PFM phase pattern on a 45 nm thick layer exfoliated on a Au-coated SiO$_2$/Si substrate, with the outer (inner) box area written by +12 V (−11 V) tip bias (with Au grounded), is shown in Figure 1c. While electrostatic effects due to possible tip-injected charges can contribute to the observed phase contrast, such charges dissipate typically within 0.5 h even in insulators (e.g., ≈1000 s in HfO$_2$),[36] and are expected to have a shorter lifetime in more conducting materials such as semiconducting α-In$_2$Se$_3$. The phase patterns observed in our studies persisted for at least 24 h, suggesting minimal electrostatic effects. We have also observed the IP piezoresponse, albeit rather weak, together with the OOP signal (Figure S1; Supporting Information). One possible reason for the weak IP signal, in contrast to previous studies, is that our instrument might not be optimized to detect IP response. Nonetheless, our observations, particularly the changes to the OOP polarization through an IP electric field (see below), support the OOP-IP interlink. OOP phase loops (Figure 1d), acquired from another layer (≈65 nm thick) exfoliated on Au, show clear hysteresis and ≈180° flips, confirming ferroelectricity. Additional OOP phase
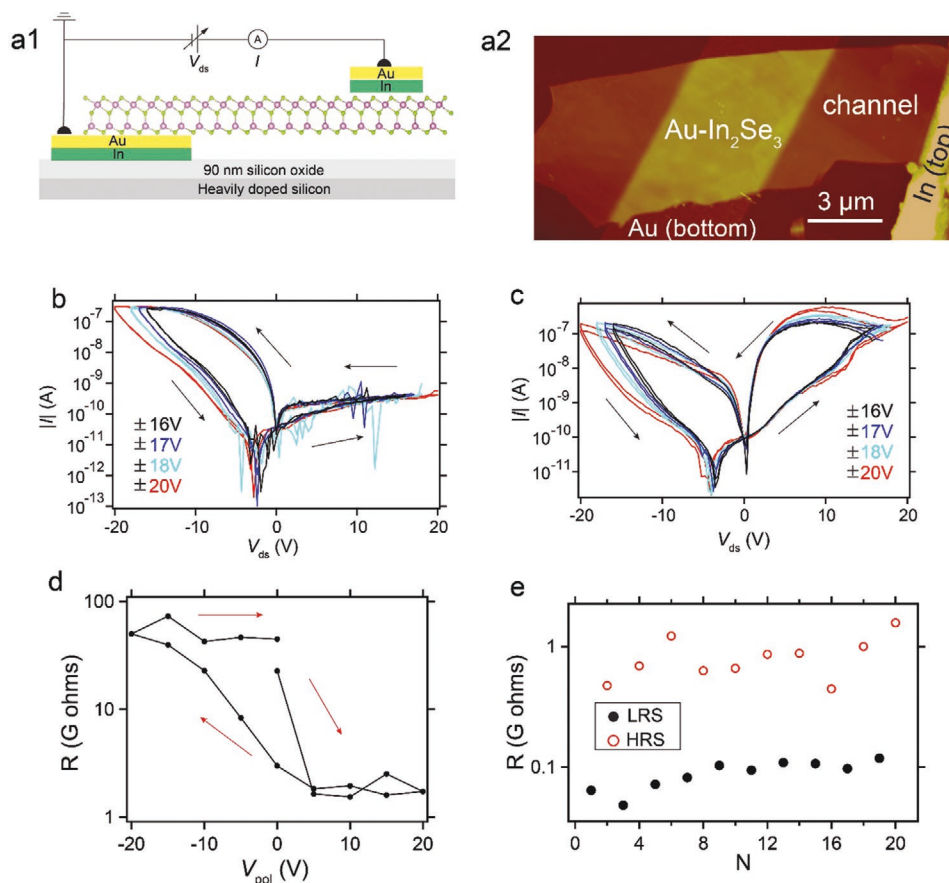
Figure 2. Device characteristics of α-In$_2$Se$_3$ ferroelectric memristors. a1) Schematic device structure of α-In$_2$Se$_3$ memristor, with the AFM image of a device shown in (a2). Hysteretic $|I|$–V_{ds} loops of b) rectifying and c) symmetric devices with increasing maximum V_{ds}. d) Device resistance (R) loop measured at −0.6 V from a rectifying device as a function of the poling voltage (V_{pol}). e) Switching of the device resistance (R) measured at −1.6 V from a rectifying device over 20 cycles of poling.

loops obtained from layers with various thicknesses show an increasing coercive voltage with increasing layer thickness (Figure S2; Supporting Information), consistent with a constant coercive field. It is important to note that hysteresis loops can also be observed from layers on bare SiO$_2$ (90 nm)/Si with the heavily doped Si grounded (Figure S3; Supporting Information); this allows us to directly probe the domain orientations of our devices and correlate those with the device characteristics (see also below).

Our planar memristors consist of mechanically exfoliated α-In$_2$Se$_3$ layers with bottom and top electrodes, as shown schematically in **Figure 2** a1 together with an atomic force microscopy (AFM) image shown in Figure 2 a2. The motivation for the asymmetric electrodes, i.e., Au (bottom) versus In (top), is to isolate the device response to only one electrode (i.e., Au) to facilitate the studies of device switching mechanisms. Particularly, the top In electrode, with a low work function of ≈4.09 eV, is expected to always behave as an ohmic contact[37] to the n-type α-In$_2$Se$_3$ and therefore would have minimal impact on the memristor response upon polarization switching. On the other hand, the bottom Au electrode, with a large work function (≈5.4 eV), forms a Schottky contact to α-In$_2$Se$_3$, and, per the common assumption, polarization reversal would lead to

significant changes to the Schottky barrier height and thus the device resistance. In addition, the bottom configuration of the Au electrode allows for direct access to the metal-ferroelectric interface region. With this electrode configuration, the electric field established by external biases across the device is predominantly IP with a negligible (≈1%) OOP component (Figure S4; Supporting Information).

With the bottom (top) electrode grounded (biased), the as-fabricated devices exhibit two types of current–voltage (I–V_{ds}) relations: rectifying and symmetric, as shown in Figure 2b,c, respectively. Both types of behaviors are expected as the as-exfoliated layers can have either up or down polarizations, leading to different Schottky barrier heights at the In$_2$Se$_3$-Au interface; particularly, a higher (lower) Schottky barrier corresponding to the rectifying (symmetric) I–V_{ds} relation.[38] We note that, for the rectifying I–V_{ds}, the negative bias to the In electrode (i.e., negative V_{ds}) represents the forward bias condition with the larger current, consistent with the Schottky (ohmic) contact at the In$_2$Se$_3$-Au (In$_2$Se$_3$-In) interface as expected. Pinched I–V_{ds} hysteresis loops were observed from both types of devices (Figure 2b,c), with each loop consisting of two round sweeps of V_{ds} (i.e., $+V_{ds,\,max} \rightarrow -V_{ds,\,max} \rightarrow +V_{ds,\,max} \rightarrow -V_{ds,\,max} \rightarrow +V_{ds,\,max}$, where $V_{ds,\,max}$ is the maximum V_{ds}). Such pinched (at the origin)

loops are characteristic of memristive behaviors.[5] The top (bottom) of the loop corresponds to the low-resistance (high-resistance) state, i.e., LRS and HRS. As indicated by the arrows in Figure 2c, for the device with the symmetric I–V_{ds}, it starts with LRS when the sweep begins from $+V_{ds, max}$; as V_{ds} reaches $-V_{ds, max}$, the device is switched into HRS and maintains this state until V_{ds} sweeps into the positive bias region, at which point the device reverts back to LRS, exhibiting two pinched loops in both positive and negative bias regions. Notably, the rectifying device shows the pinched I–V_{ds} loop only under forward bias condition (Figure 2b); i.e., the switching between LRS and HRS has a weak effect on the I–V_{ds} relation under the reverse bias condition, where the current transport is limited by the metal-ferroelectric Schottky barrier. This indicates a lack of impact from the ferroelectric polarization reversal on the Schottky barrier height (see also below).

These devices demonstrate a large switching ratio between HRS and LRS of $\approx 10^3$ at certain biases, comparable to results from a previous report of In_2Se_3 memristors[33] and larger than the ferroelectric tunnel junction-based memristors.[5] As In_2Se_3 can exist in multiple crystalline phases,[39] it is necessary to rule out structural phase transitions as a possible device switching mechanism. We conducted spatially resolved Raman spectroscopy on a device in LRS and HRS (Figure S5; Supporting Information), which shows that the crystal lattice remains in the α phase after the switching. The memristive characteristics are further demonstrated in Figure 2d: the resistance (R) of a rectifying device, measured at $V_{ds} = -0.6$ V, exhibits a hysteresis loop as a function of the poling voltage (V_{pol}) and continuously tunable device resistance states. We have also conducted repeated

poling using ± 20 V pulses (with a duration of 15 s), and R measured at -1.6 V shows reproducible switching (Figure 2e) with the positive (negative) voltage pulse converting the device into LRS (HRS). Additional switching of another device for 60 cycles is shown in Figure S6 (Supporting Information), where poling voltages of ± 5 V with ≈ 1 s duration were used. The bipolar nature of the switching, i.e., voltage pulses with opposite polarities are necessary to switching between HRS and LRS, is consistent with the ferroelectric polarization reversal as the origin of the resistive switching. The LRS/HRS currents remain stable over 1000 s, as shown in Figure S7 (Supporting Information).

To gain microscopic insights into the memristive switching behaviors, we conducted OOP-PFM and Kelvin probe force microscopy (KPFM) on devices in HRS and LRS. The open device structure allows us to directly access the ferroelectric domain configurations and the surface electric potential in the device channel and the In_2Se_3-Au interface region. The I–V_{ds} relations corresponding to LRS and HRS of a rectifying device are shown in **Figure 3**a,d, respectively. In LRS, the entire device area, including the channel region and the In_2Se_3-Au interface, shows uniform polarization orientation (Figure 3b); i.e., the device is in the monodomain state. However, the contact potential difference (CPD) mapping reveals regions with different surface electric potentials. Particularly, the In_2Se_3-Au interface has a lower potential than the channel region, corresponding to a higher work function in the interface than the channel. In light of the monodomain state, this indicates the presence of a Schottky barrier between In_2Se_3 and Au (**Figure 4**; see also below), consistent with the rectifying I–V_{ds} relation. As the device is switched into HRS, ferroelectric domains with
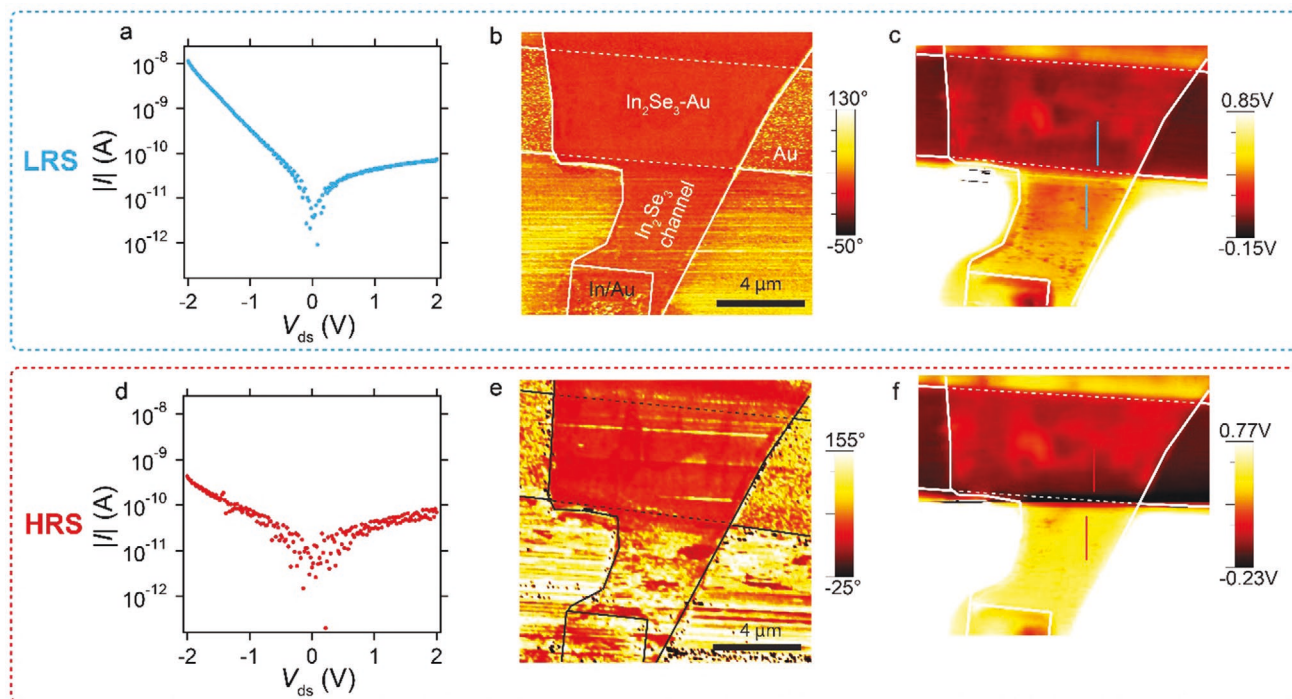

Figure 3. Correlation among device resistance, ferroelectric domains, and surface potentials. $|I|$–V_{ds} relation, OOP PFM phase image, and CPD image of a rectifying device in a–c) LRS, respectively, in blue dashed box] and d–f) HRS, respectively, in red dashed box]. The solid blue (red) lines in (c,f) represent the locations from which the line profiles were obtained (see Figure 4).
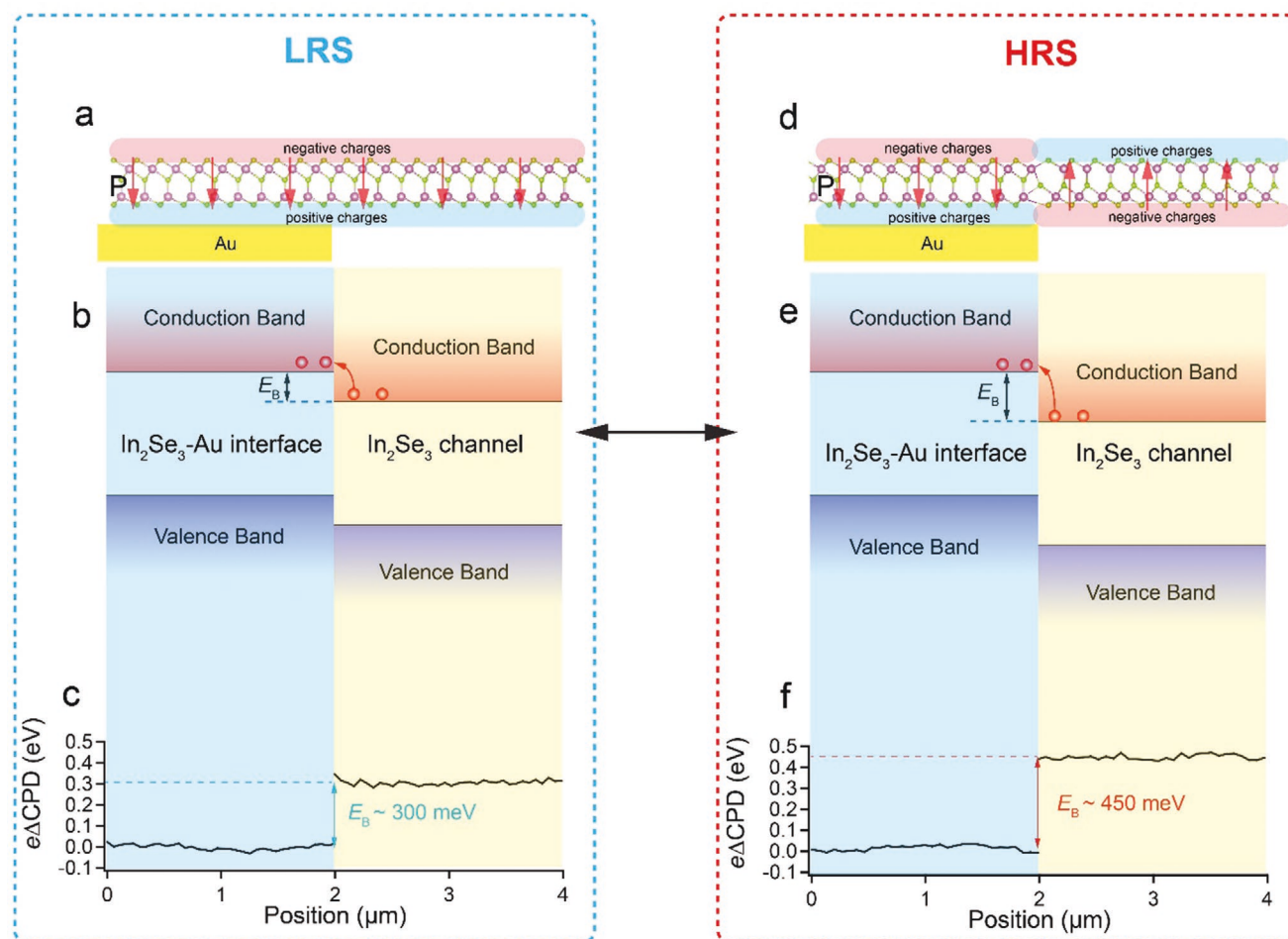
ADVANCED
SCIENCE NEWS
www.advancedsciencenews.com

ADVANCED
FUNCTIONAL
MATERIALS
www.afm-journal.de

Figure 4. Microscopic origin of the ferroelectric switching. Schematic ferroelectric domain configurations, band alignment between domains, and experimentally measured difference in surface potential energy between domains of the memristor in a–c) LRS, respectively, in blue dashed box] and d–f) HRS, respectively, in red dashed box].

different polarization orientations emerged (Figure 3e). Interestingly, the polarization at the In_2Se_3-Au interface remains largely unchanged, while significant (but not uniform; see also below) polarization reversal can be observed in the channel region. Concurrent with the polarization flipping, the surface electric potential increases substantially in the channel region, while showing little variations (and thus the Schottky barrier height) in the interface region (Figure 3c,f). A device with the symmetric I–V_{ds} relation exhibits similar behaviors (Figure S8; Supporting Information). Additional experiments, where the top (bottom) electrode was grounded (biased), also show the polarization reversal in the device channel region, and the In_2Se_3-Au interface largely retains its polarization state (Figure S9; Supporting Information).

The lack of significant polarization reversal at the In_2Se_3-Au interface during switching is significant, as it contradicts the assumption of polarization flipping at the metal-ferroelectric interface as the resistive switching mechanism. We contribute this to the strong internal electric field associated with the Schottky barrier at the In_2Se_3-Au interface, which "locks" the ferroelectric polarization. On the other hand, the OOP polarization in the channel region is flipped by the external

IP electric field applied to the device. The absence of polarization reversal, and the lack of changes to the Schottky barrier height at the In_2Se_3-Au interface, are consistent with the similar I–V_{ds} characteristics under the reverse biases in both LRS and HRS (Figure 3a,d), where the reverse current is limited by the Schottky barrier height. With the device channel region as the switch-active element, we suggest that the change in the band offset between In_2Se_3-Au interface and the In_2Se_3 channel is responsible for the LRS ↔ HRS switching. As illustrated in Figure 4b, in the monodomain state corresponding to LRS, there exists an energy barrier, E_B that arises from the band misalignment between the interface and the channel. This energy barrier can be measured from the line profiles of the surface potentials in the interface and the channel region (Figure 3c). The line profiles are plotted as $e\Delta$CPD (where e is the fundamental charge) in Figure 4c, with the surface potential of the interface as the reference, from which $E_B \approx 300$ meV can be measured. This barrier impedes electron flow from the channel into the interface under the forward biases. As the device is switched into HRS, E_B increases to ≈450 meV, as shown in Figures 3f and 4f; such an increase leads to higher device resistances. Assuming the thermionic emission model,

**ADVANCED
SCIENCE NEWS**
www.advancedsciencenews.com

**ADVANCED
FUNCTIONAL
MATERIALS**
www.afm-journal.de

the ratio of the forward currents in LRS and HRS, I_{LRS}/I_{HRS}, is proportional to $\exp(\Delta E_B/kT)$. With $\Delta E_B \approx 150$ meV, I_{LRS}/I_{HRS} is ≈ 320, which is within the range of the switching ratio we have observed (Figure 2b,c). In a previous study of planar In_2Se_3 ferroelectric memory,[33] an apparent barrier height change (where the barrier was assumed to be located between In_2Se_3 and Au) was determined from modeling the $I-V_{ds}$ curves to be $\approx 100-200$ meV, in agreement with our results.

We next discuss the relation between the changes in E_B and the polarization reversal. Because of the interlinked IP-OOP polarizations, a change of OOP polarization in the channel region indicates a simultaneous IP polarization flipping. Opposite IP polarizations between domains result in charged domain walls,[40] and the surface potential variations are thus only expected at the domain boundaries, inconsistent with our observation of surface potential changes across the entire channel region. On the other hand, surface bound charges due to OOP polarization can modify the surface potentials, as illustrated in Figure 4a,d. Particularly, in the channel region, as the polarization is flipped upward, the surface charges at the upper surface become positive, leading to downward surface band bending, corresponding to a smaller work function and a larger E_B. We note that the polarization reversal occurs across most of the channel region but is not entirely uniform (Figure 3e and Figure S8: Supporting Information). This inhomogeneity is consistent with and necessary to the memristive switching, as the continuous tunability of the device resistance requires a gradual evolution of ferroelectric domain configurations,[5] which is largely controlled by domain wall dynamics. Further studies are required to correlate the history of the poling voltage pulses, domain nucleations, and the domain wall motions to establish a deeper understanding of the memristive behaviors. On the other hand, the surface potential shows rather uniform distributions; we attribute this to the long-range electrostatic interactions, in contrast to the short-range mechanical forces in PFM that limit the spatial resolution of KPFM.

3. Conclusion

In summary, we demonstrate thin planar ferroelectric memristors based on van der Waals In_2Se_3 that exhibit continuously tunable resistance states through an application of an IP electric field. Using correlated PFM and KPFM studies, the formation of energy barriers between ferroelectric domains has been revealed to be responsible for the device resistance switching. These findings establish the microscopic operating mechanisms of memristive switching in a unique van der Waals ferroelectric material with interlinked OOP-IP polarizations, critical to future development of ultrathin and novel memory devices for information storage and processing applications.

4. Experimental Section

Device Fabrication: Thin bottom electrodes (15 nm In/15 nm Au) were patterned through e-beam lithography and deposited on SiO_2 (90 nm)/Si Substrates (University Wafers) using a physical deposition system (NEXDEP from Angstrom Engineering). During deposition a tungsten (tungsten-coated aluminum) boat were used to hold In (Au) sources, respectively, with a chamber pressure of $\approx 1 \times 10^{-6}$ Torr, and a $\approx 1-2$ Å s^{-1} deposition rate. Wafers with these bottom electrodes were cleaned with plasma cleaning and buffer HF (BHF) etching before thin α-In_2Se_3 layers (purchased from 2D semiconductors) were mechanically exfoliated. Specifically, In_2Se_3 crystals were first placed on a piece of Scotch tape and then repeatedly exfoliated using multiple layers of tape. These layers were transferred to a gel film (WF-60-X4 from Gel-Pak) on a glass slide. This slide was mounted on a manual translational stage under an optical microscope. Optically identified thin, uniform layers were then exfoliated to on top of the bottom electrodes, followed by BHF cleaning. E-beam lithography and thermal evaporation were used to define top electrodes (70 nm In/60 nm Au).

Raman Spectroscopy: Raman spectra were taken with a confocal InVia Raman microscope (Renishaw) using a 633 nm He–Ne laser. The laser was focused on the samples through a 6.5 mm working distance Nikon microscope objective (100 ×, NA = 0.7). A laser power of ≈ 0.4 mW was used during the spectroscopic measurements. To measure the Raman spectra under parallel and perpendicular polarizations a linear polarizer and half-wave plate were inserted into the beam path directly before the CCD detector.

Electrical Characterizations: Current–voltage relations of fabricated devices were measured using a Jmicro Technology LMS 2709 probe station. Electrodes were biased through a Precision Source/Measure Unit (Keysight B2902A). To pole the device into the high- and low-resistance states, a constant voltage of ±20 V with 15 s duration was applied to the top electrode, unless otherwise noted in the text.

PFM and KPFM: Surface topography, PFM, and KPFM measurements were conducted in ambient air with a Bruker Multimode 8 atomic force microscope using a Bruker NanoScope V controller. Advanced TEC AFM probes with PtIr5 coating (NANOSENSORS) and a 0.7–9 N m^{-1} force constant were used in all scans. During PFM measurements, the piezoresponse phase channel was locked in at the tip/sample resonant frequency of ≈ 270 kHz using a 500 mV AC drive amplitude. Frequency modulated KPFM with the dual-pass mode was used to obtain surface topography in the first pass and then surface potential with a lift height of 50 nm in the second pass.

Supporting Information

Supporting Information is available from the Wiley Online Library or from the author.

Conflict of Interest

The authors declare no conflict of interest.

[1] D. J. Jung, F. D. Morrison, M. Dawber, H. H. Kim, K. Kim, J. F. Scott, *J. Appl. Phys.* **2004**, *95*, 4968.

[2] A. I. Kingon, J. P. Maria, S. K. Streiffer, *Nature* **2000**, *406*, 1032.

[3] V. Garcia, M. Bibes, *Nat. Commun.* **2014**, *5*, 4289.

[4] S. Mathews, R. Ramesh, T. Venkatesan, J. Benedetto, *Science* **1997**, *276*, 238.

[5] A. Chanthbouala, V. Garcia, R. O. Cherifi, K. Bouzehouane, S. Fusil, X. Moya, S. Xavier, H. Yamada, C. Deranlot, N. D. Mathur, M. Bibes, A. Barthelemy, J. Grollier, *Nat. Mater.* **2012**, *11*, 860.

[6] S. Boyn, J. Grollier, G. Lecerf, B. Xu, N. Locatelli, S. Fusil, S. Girod, C. Carretero, K. Garcia, S. Xavier, J. Tomas, L. Bellaiche, M. Bibes, A. Barthelemy, S. Saighi, V. Garcia, *Nat. Commun.* **2017**, *8*, 14736.

[7] J. Junquera, P. Ghosez, *Nature* **2003**, *422*, 506.

[8] V. Nagarajan, S. Prasertchoung, T. Zhao, H. Zheng, J. Ouyang, R. Ramesh, W. Tian, X. Q. Pan, D. M. Kim, C. B. Eom, H. Kohlstedt, R. Waser, *Appl. Phys. Lett.* **2004**, *84*, 5225.

[9] C. Lichtensteiger, J. M. Triscone, J. Junquera, P. Ghosez, *Phys. Rev. Lett.* **2005**, *94*, 047603.

[10] K. Chang, T. P. Kaloni, H. C. Lin, A. Bedoya-Pinto, A. K. Pandeya, I. Kostanovskiy, K. Zhao, Y. Zhong, X. P. Hu, Q. K. Xue, X. Chen, S. H. Ji, S. Barraza-Lopez, S. S. P. Parkin, *Adv. Mater.* **2019**, *31*, 1804428.

[11] Y. Bao, P. Song, Y. P. Liu, Z. H. Chen, M. L. Zhu, I. Abdelwahab, J. Su, W. Fu, X. Chi, W. Yu, W. Liu, X. X. Zhao, Q. H. Xu, M. Yang, K. P. Loh, *Nano Lett.* **2019**, *19*, 5109.

[12] R. X. Fei, W. Kang, L. Yang, *Phys. Rev. Lett.* **2016**, *117*, 097601.

[13] A. Belianinov, Q. He, A. Dziaugys, P. Maksymovych, E. Eliseev, A. Borisevich, A. Morozovska, J. Banys, Y. Vysochanskii, S. V. Kalinin, *Nano Lett.* **2015**, *15*, 3808.

[14] F. C. Liu, L. You, K. L. Seyler, X. B. Li, P. Yu, J. H. Lin, X. W. Wang, J. D. Zhou, H. Wang, H. Y. He, S. T. Pantelides, W. Zhou, P. Sharma, X. D. Xu, P. M. Ajayan, J. L. Wang, Z. Liu, *Nat. Commun.* **2016**, *7*, 12357.

[15] S. G. Yuan, X. Luo, H. L. Chan, C. C. Xiao, Y. W. Dai, M. H. Xie, J. H. Hao, *Nat. Commun.* **2019**, *10*, 1775.

[16] Z. Y. Fei, W. J. Zhao, T. A. Palomaki, B. S. Sun, M. K. Miller, Z. Y. Zhao, J. Q. Yan, X. D. Xu, D. H. Cobden, *Nature* **2018**, *560*, 336.

[17] M. W. Si, A. K. Saha, S. J. Gao, G. Qiu, J. K. Qin, Y. Q. Duan, J. Jian, C. Niu, H. Y. Wang, W. Z. Wu, S. K. Gupta, P. D. D. Ye, *Nat. Electron.* **2019**, *2*, 580.

[18] M. W. Si, A. K. Saha, P. Y. Liao, S. J. Gao, S. M. Neumayer, J. Jian, J. K. Qin, N. B. Wisinger, H. Y. Wang, P. Maksymovych, W. Z. Wu, S. K. Gupta, P. D. Ye, *ACS Nano* **2019**, *13*, 8760.

[19] X. D. Wang, C. S. Liu, Y. Chen, G. J. Wu, X. Yan, H. Huang, P. Wang, B. B. Tian, Z. C. Hong, Y. T. Wang, S. Sun, H. Shen, T. Lin, W. D. Hu, M. H. Tang, P. Zhou, J. Wang, J. J. Sun, X. J. Meng, J. H. Chu, Z. Li, *2D Mater.* **2017**, *4*, 065121.

[20] M. W. Si, P. Y. Liao, G. Qiu, Y. Q. Duan, P. D. D. Ye, *ACS Nano* **2018**, *12*, 6700.

[21] C. Gong, E. M. Kim, Y. Wang, G. Lee, X. Zhang, *Nat. Commun.* **2019**, *10*, 2657.

[22] F. Xue, Z. Wang, Y. S. Hou, L. Gu, R. Q. Wu, *Phys. Rev. B* **2020**, *101*, 184426.

[23] L. Z. Li, B. Z. Zhou, *J. Mater. Chem. C* **2020**, *8*, 4534.

[24] X. K. Huang, G. N. Li, X. Nie, X. P. Jiang, J. M. Liu, *Phys. Rev. B* **2019**, *100*, 235445.

[25] Y. Zhou, D. Wu, Y. H. Zhu, Y. J. Cho, Q. He, X. Yang, K. Herrera, Z. D. Chu, Y. Han, M. C. Downer, H. L. Peng, K. J. Lai, *Nano Lett.* **2017**, *17*, 5508.

[26] C. J. Cui, W. J. Hu, X. G. Yan, C. Addiego, W. P. Gao, Y. Wang, Z. Wang, L. Z. Li, Y. C. Cheng, P. Li, X. X. Zhang, H. N. Alshareef, T. Wu, W. G. Zhu, X. Q. Pan, L. J. Li, *Nano Lett.* **2018**, *18*, 1253.

[27] J. Xiao, H. Y. Zhu, Y. Wang, W. Feng, Y. X. Hu, A. Dasgupta, Y. M. Han, Y. Wang, D. A. Muller, L. W. Martin, P. A. Hu, X. Zhang, *Phys. Rev. Lett.* **2018**, *120*, 227601.

[28] C. X. Zheng, L. Yu, L. Zhu, J. L. Collins, D. Kim, Y. D. Lou, C. Xu, M. Li, Z. Wei, Y. P. Zhang, M. T. Edmonds, S. Q. Li, J. Seidel, Y. Zhu, J. Z. Liu, W. X. Tang, M. S. Fuhrer, *Sci. Adv.* **2018**, *4*, eaar7720.

[29] W. J. Ding, J. B. Zhu, Z. Wang, Y. F. Gao, D. Xiao, Y. Gu, Z. Y. Zhang, W. G. Zhu, *Nat. Commun.* **2017**, *8*, 14956.

[30] S. Y. Wan, Y. Li, W. Li, X. Y. Mao, W. G. Zhu, H. T. Zeng, *Nanoscale* **2018**, *10*, 14885.

[31] F. Xue, W. J. Hu, K. C. Lee, L. S. Lu, J. W. Zhang, H. L. Tang, A. Han, W. T. Hsu, S. B. Tu, W. H. Chang, C. H. Lien, J. H. He, Z. D. Zhang, L. J. Li, X. X. Zhang, *Adv. Funct. Mater.* **2018**, *28*, 1803738.

[32] M. J. Dai, K. Li, F. K. Wang, Y. X. Hu, J. Zhang, T. Y. Zhai, B. Yang, Y. Q. Fu, W. W. Cao, D. C. Jia, Y. Zhou, P. A. Hu, *Adv. Electron. Mater.* **2020**, *6*, 1900975.

[33] F. Xue, X. He, J. R. D. Retamal, A. L. Han, J. W. Zhang, Z. X. Liu, J. K. Huang, W. J. Hu, V. Tung, R. H. He, L. J. Li, X. X. Zhang, *Adv. Mater.* **2019**, *31*, 1901300.

[34] H. Kohlstedt, A. Petraru, K. Szot, A. Rudiger, P. Meuffels, H. Haselier, R. Waser, V. Nagarajan, *Appl. Phys. Lett.* **2008**, *92*, 062907.

[35] J. Igo, S. W. Zhou, Z. G. Yu, O. P. Amnuayphol, F. Zhao, Y. Gu, *J. Phys. Chem. C* **2018**, *122*, 22849.

[36] N. Balke, P. Maksymovych, S. Jesse, KravchenkoII, Q. Li, S. V. Kalinin, *ACS Nano* **2014**, *8*, 10229.

[37] Q. M. Wang, L. L. Yang, S. W. Zhou, X. J. Ye, Z. Wang, W. G. Zhu, M. D. McCluskey, Y. Gu, *J. Phys. Chem. Lett.* **2017**, *8*, 2887.

[38] Due to the mechanical exfoliation process, the initial polarization direction of as-exfoliated layers is random, which leads to the non-uniform device performance, particularly the rectifying vs. the symmetric current-voltage relations. This issue can be addressed by the recent advances (e.g., Poh, et al., *Nano Lett. 2018, 18*, 6340) in the growth of large-area In_2Se_3 thin films with highly uniform crystal orientations (which, in the case of In_2Se_3, determines the ferroelectric polarization direction).

[39] X. Tao, Y. Gu, *Nano Lett.* **2013**, *13*, 3501.

[40] P. Schoenherr, K. Shapovaloy, J. Schaab, Z. Yan, E. D. Bourret, M. Hentschel, M. Stengel, M. Fiebig, A. Cano, D. Meier, *Nano Lett.* **2019**, *19*, 1659.